Supplement of Biogeosciences, 19, 5953–5972, 2022
https://doi.org/10.5194/bg-19-5953-2022-supplement

Biogeosciences Open Access EGU

Supplement of

Using atmospheric observations to quantify annual biogenic carbon dioxide fluxes on the Alaska North Slope

Luke D. Schiferl et al.

Correspondence to: Luke D. Schiferl (schiferl@ldeo.columbia.edu)

S1 Determining Tundra Vegetation Photosynthesis and Respiration Model (TVPRM) variable parameters using observed net CO_2 flux

The TPVRM variable parameters (α_s [units: μmol CO_2 m^{-2} s^{-1} °C^{-1}], β_s [μmol CO_2 m^{-2} s^{-1}], α_a [μmol CO_2 m^{-2} s^{-1} °C^{-1}], β_a [μmol CO_2 m^{-2} s^{-1}], λ [μmol CO_2 m^{-2} s^{-1} (μmol photon m^{-2} s^{-1} mW m^{-2} nm^{-1} sr^{-1}) $^{-1}$], and PAR_0 [μmol photon m^{-2} s^{-1}] are calculated for each 365-day period using a moving window (i.e., day 1–365, day 2–366, day 3–367, etc.) for 2013 to 2017 as follows:

Step 1: *Linear regression of observed net CO_2 flux against soil temperature (T_s) during non-growing season to determine α_s and β_s and calculate soil respiration (R_{soil}).* Daily mean T_s and the corresponding daily mean observed net CO_2 flux during potential non-growing days (daily maximum air temperature (T_a) < 0°C) when SIF = 0 and 50% of the half-hours have observed net CO_2 flux are identified and sorted into 5% bins by ordering the daily mean T_s. Regression is performed on the 20 median observed net CO_2 flux and T_s values calculated from these bins. Daily values are used here to account for the lack of variability in T_s from reanalysis products on sub-daily timescales. The binning approach distributes the influence of low-end T_s values more evenly in the regression, which is needed because the distribution of T_s values is non-normal, with a majority of points just below 0°C during the long zero-curtain period.

Step 2: *Linear regression of observed net CO_2 flux against T_a during growing-season night to determine α_a and β_a and calculate plant respiration (R_{plant}).* Half-hourly T_a and the corresponding half-hourly observed net CO_2 flux with R_{soil} (calculated in step 1) removed during potential growing days (daily minimum T_a > 0°C) when solar-induced chlorophyll fluorescence (SIF) > 0 and photosynthetically active radiation (PAR) <= 4 μmol photon m^{-2} s^{-1} are identified and sorted into 5% bins by ordering the half-hourly T_a. Regression is performed on the 20 median observed net CO_2 flux with R_{soil} removed and T_a values calculated from these bins. The binning approach distributes the influence of T_a values more evenly in the regression, which is needed because distribution of values is sporadic and variable as data from the light-limited growing season is limited to August and the number of total points available is only ~10% of those used in the R_{soil} fit.

Step 3: *Nonlinear fitting of observed net CO_2 flux against PAR, SIF, and T_a during growing-season day to determine λ and PAR_0 and calculate gross primary productivity (GPP).* Fitting is performed using nonlinear least squares (nls) on the half-hourly observed net CO_2 flux with R_{soil} and R_{plant} (calculated in steps 1 and 2, respectively) removed and half-hourly PAR, SIF (constant daily value) and T_a (used to calculate the temperature scalar (T_{scale}) from the potential growing days when SIF > 0 and PAR > 4 μmol photon m^{-2} s^{-1}. Initial values for nls are PAR_0 = 240 and λ = 0.04, which were reported as shrub tundra parameter values by Luus et al. (2017).

Each 365-day period must have valid data (observed net CO_2 flux, reanalyzed T_a, T_s and PAR, and derived SIF) for 70% of potential growing days and 50% of potential non-growing days in order for variable parameters to be calculated. This requirement is most often failed due to gaps in the observed net CO_2 flux. In order to mitigate unrealistic observed non-growing season uptake outside of noise, prior to step 1, we remove half-hourly observed net CO_2 flux values during 24-hour periods on

non-growing days when 50% of half-hours have observed net CO_2 flux and both 50% and the mean of those observed net CO_2 flux values are negative. For each step, data are removed when net CO_2 flux values are outside of three standard deviations of the mean.

The moving window method accounts for variability in both day-to-day data availability and year-to-year ecosystem response to environmental drivers (parameterization). The median value for each variable parameter from the set of valid 365-day periods is used in the site-level net CO_2 flux evaluation (see Sect. S4, Fig. S4) and regional scaling. These median variable parameters are determined for each combination of input reanalysis meteorology and SIF product at each eddy covariance flux tower site.

The main components of the procedures for steps 1-3 above (i.e., linear regressions respiration, non-linear regression for GPP) largely follow that of the previous version of this empirical CO_2 flux model described by Luus et al. (2017). However, instead of using snow cover as the indicator of T_a-driven total respiration (no snow) or T_s-driven total respiration (snow), as in Luus et al. (2017), we separate respiration into R_{soil} and R_{plant} components, which explicitly represent heterotrophic and autotrophic respiration communities, respectively. R_{soil} is now applied year-round, with R_{plant} applied during the growing season as determined by SIF. This change also simplifies the required model inputs to only reanalysis data and SIF.

The threshold criteria described above for performing a regression calculation during a particular window and for filtering data used in the regressions were chosen to balance maintaining representativeness of the various regressions (i.e., data is available from throughout the entire time period) and keeping enough data to be useful for a stable fit (i.e., non-growing season data is more limited). The methods for determining the TPVRM parameters described here also result in the best version of the model compared to observations after many development iterations.

S2 Meteorological reanalysis and other T_s products used by TVPRM

Meteorological reanalysis products used by TPVRM are shown in Table S4. Downward shortwave radiation product (dswrf, ssrd) values are converted to PAR using a conversion factor of 1.98. Meteorology values are linearly interpolated to half-hourly (T_a, PAR) and averaged to daily (T_s) for model parameter calculation and site-level net CO_2 flux evaluation. NARR values are linearly interpolated to hourly for regional simulations. Site-level calculations are made using values from the meteorological product gridbox corresponding to site location. Meteorological product horizontal resolution is maintained for regional simulations.

For TVPRM simulations driven by T_s from the Remote Sensing driven Permafrost Model (RS-PM (Yi et al., 2018, 2019)), we linearly interpolate RS-PM T_s from 8 day to daily values and horizontally regrid from 1 km to match the other meteorological data by averaging all native pixel center points within each meteorological reanalysis product gridbox. When sub-daily RS-PM T_s is needed to calculate the simulated net CO_2 flux, we apply a constant value. We tested the use of all RS-PM T_s depths from 1 cm to 105 cm and found varying performance, with T_s from deeper layers improving the TVPRM

performance at sites with greater soil thickness. For consistent comparison to NARR, we use RS-PM T_s at 8 cm depth in our analysis here.

We also tested using multi-layer fit driven by soil column temperature. In this approach, we summed the degrees above a freezing threshold (-0.75°C at IVO, -5°C at CMDL) representing the zero-curtain time period for each layer, multiplied by the layer thickness. This column sum temperature above freezing was used in place of the single layer T_s above in the same linear fit process to determine parameters which represent R_{soil}. While likely more realistic in driving R_{soil} than a single layer approach, applying the multi-layer sum to our constrained TVPRM member did not result in significantly higher early cold season (Sep–Dec) CO_2 emissions needed to match the observations since both cases match well to the eddy flux measurements.

S3 SIF products used by TVPRM

SIF products used by TPVRM are shown in Table S5. GOSIF and CSIF are linearly interpolated to daily values and horizontally regridded by averaging all native pixel center points within each meteorological reanalysis product gridbox. Any resulting negative values for all products are set to 0. Site-level SIF values correspond to the site latitude (GOME-2) or site location within a meteorology gridbox (GOSIF, CSIF). Regional simulation GOME-2 values correspond to the meteorology gridbox center point latitude.

S4 Evaluation of site-level net CO_2 flux against observations

We calculate the TVPRM net CO_2 flux at half-hourly time resolution using the median variable parameters determined above for each eddy flux site for each combination of reanalysis meteorology and SIF product. We then evaluate the simulated net CO_2 flux against the observed net CO_2 flux for each eddy flux site over various averaging lengths (half-hour, one day, two weeks) for various timeframes (year-round, growing season, non-growing season). Elements of this evaluation are shown in Fig. S4. For this evaluation, we calculated the coefficient of determination (R^2) as the square of the Pearson correlation coefficient for all points. The slope (m) is determined by ordinary least squares using the median of each 10% bin of ordered observed and corresponding simulated net CO_2 flux. The normalized mean bias (NMB) of all points is defined as $\frac{\sum(\text{simulated} - \text{observed})}{\sum \text{observed}}$. The root-mean-square error (RMSE) of all points is defined as $\sqrt{(\text{simulated} - \text{observed})^2}$.

Generally, site-level TVPRM performance is greater (higher correlation, slope closer to 1, lower bias and error) in the growing season compared to the non-growing season. Performance improves in all seasons as the timescale of averaging is lengthened, with the non-growing season notably better on the two-week scale, as T_s does not fluctuate much on the half-hourly to daily scale. Intersite performance is more variable compared to the model performance trends across seasons and timescales. The relative quality of model performance at each site is likely due to the data availability for that site for a given averaging length or timeframe.

S5 Scaling TVPRM from site-level to regional net CO_2 flux

To scale from site-level to regional net CO_2 flux, we first calculate the hourly TVPRM net CO_2 flux at each meteorological gridbox for each median variable parameter set from the eight eddy flux sites. The regional simulated net CO_2 flux at each gridbox is then determined by weighting the site-specific net CO_2 flux by the fraction of each vegetation type within that gridbox based on the classifications of inland tundra, coastal tundra, other land, inland water, and ocean. For each regional simulation, we assume all inland tundra is represented by the parameterization from one of four sites (ICS, ICH, ICT, IVO) and all coastal tundra is represented by one of the remaining sites (ATQ, BES, BEO, CMDL). This method allows for separation and testing of distinct site-level responses within each group. Figure S1 shows the distinct response of TVPRM using variable parameters from these two groups as demonstrated by the cross-site evaluation. Net CO_2 fluxes from other land, inland water, and ocean areas are set to 0.

The vegetation maps used to determine the fraction of each classification are described in Table S6. We group CAVM and RasterCAVM classifications for graminoid and shrub tundra into our inland tundra classification, with wetland tundra classifications used as coastal tundra. Barren, glacier, and ice/snow classifications are set to other land, and water classifications remain separate for inland water and ocean. ABoVE LC classifications are grouped into our classification scheme by vegetation description and spatial distribution. CAVM and RasterCAVM are proportionally scaled to match ABoVE LC for other land, inland water, and ocean, so inland and coastal tundra are the only variations between the vegetation maps. Figure S5 shows the distribution and percentage of these grouped classifications within our North Slope domain.

Spatial distribution maps throughout this study are produced by rasterizing native NARR and ERA5 gridboxes to 1 km boxes on the NASA Arctic-Boreal Vulnerability Experiment (ABoVE) standard projection and grid (https://above.nasa.gov/implementation_plan/standard_projection.html) and aggregating these boxes to 30 km, consistent with the native spatial resolution. Regional flux values are calculated using gridbox fluxes on native resolution.

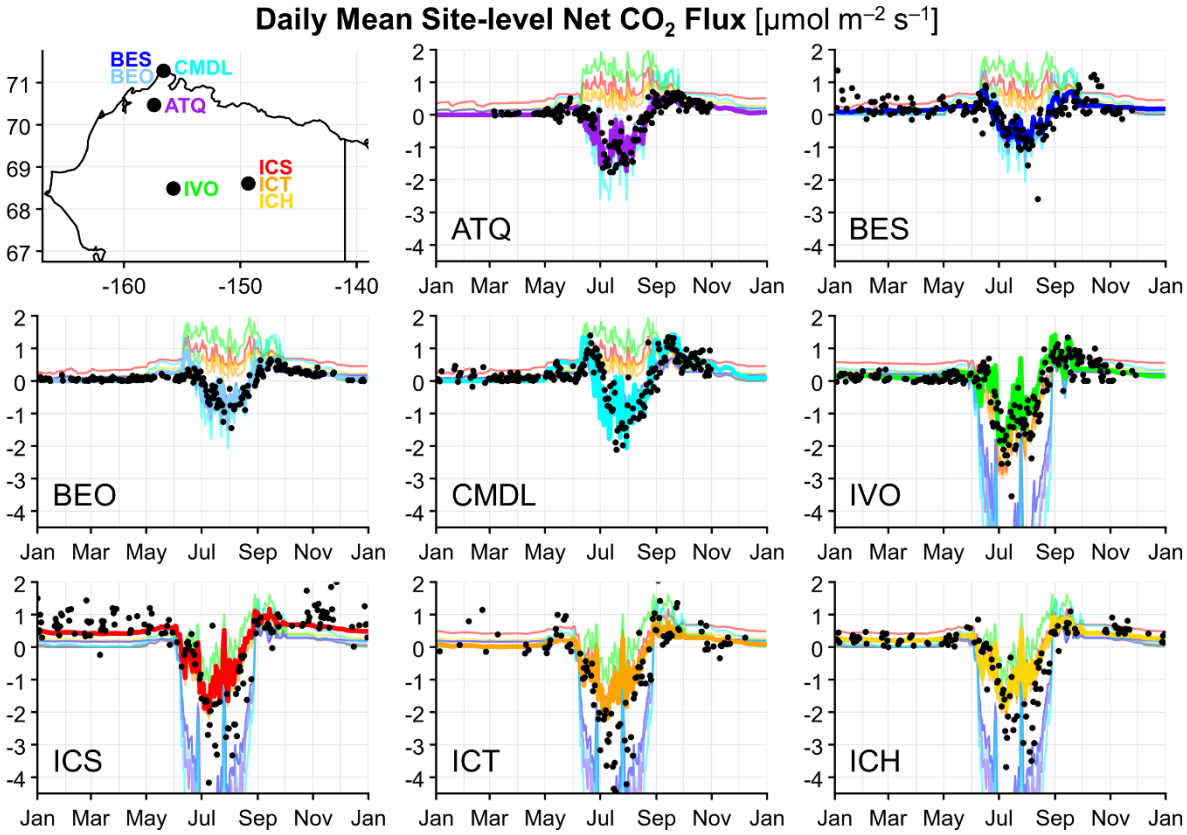

Figure S1. Timeseries of daily mean site-level net CO_2 flux for 2014 at eddy flux measurement sites on the Alaska North Slope (top left panel) used to determine TVPRM parameters. For the cross-site evaluation, each site panel uses the meteorology and SIF at that site to calculate the TVPRM simulated net CO_2 flux using the parameters determined for all sites, with the colored lines corresponding to the sites in the top left panel. Here we show TVPRM net CO_2 flux driven by NARR meteorology and the CSIF SIF product, where the net CO_2 flux for corresponding site parameters and locations are highlighted using lines with heavier weight. Black dots show observed net CO_2 flux at each site.

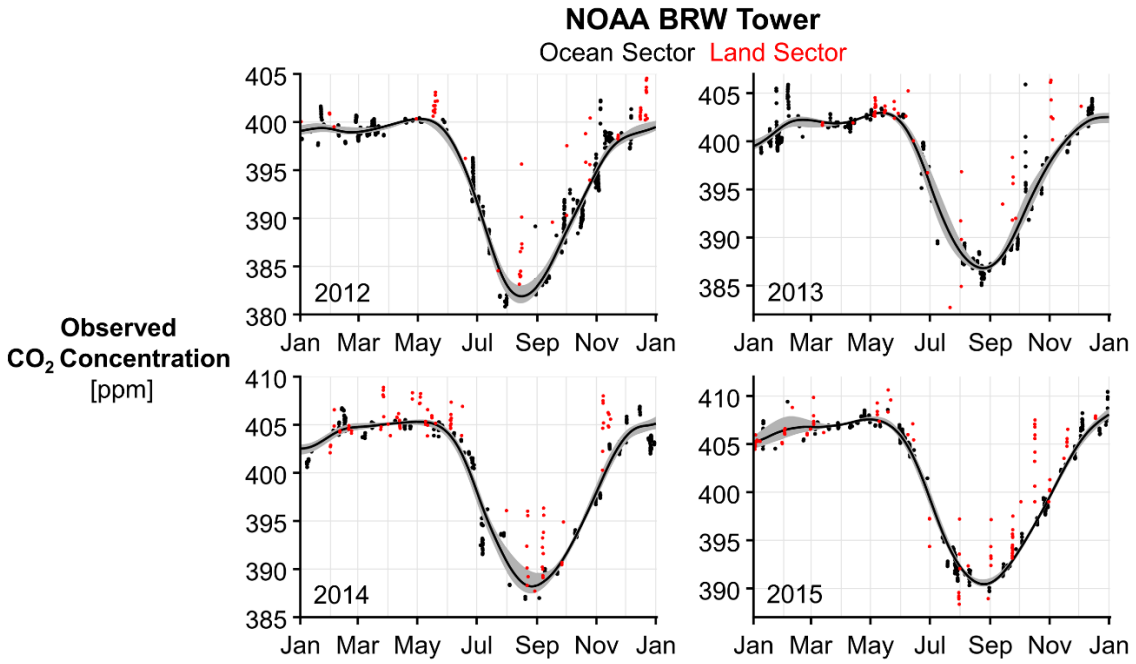

Figure S2. Timeseries of calculated NOAA BRW tower ocean sector CO_2 background concentration (black line) for 2012–2015. Uncertainty (95% of results) determined by varying start time of spline fit and repeatedly randomly removing 50% of used points shown by gray ribbon. Black dots indicate ocean sector hourly observations used in spline fit, and red dots indicate land sector hourly observations used in model evaluation (Figs. 2c–2d, 3b–3c, 4a, 4c, S11, S14).

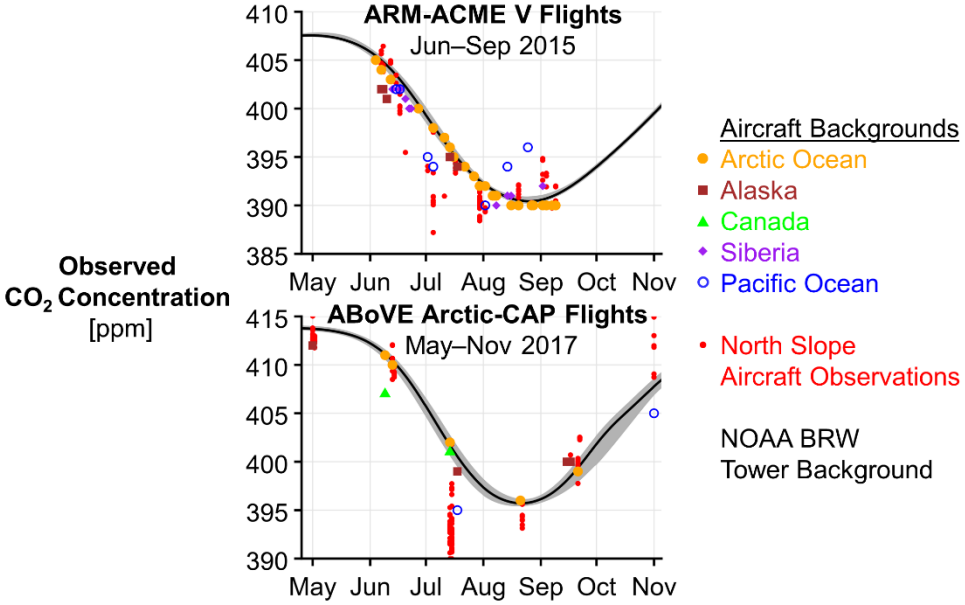

Figure S3. Timeseries of CO_2 background concentration determined using aircraft observations without Alaska North Slope surface influence for the ARM-ACME V and ABoVE Arctic-CAP flight campaigns. Various colored symbols indicate the background source region. Red dots show aircraft observations used in model evaluation (Figs. 2a–2b, 2d, S8). NOAA BRW tower ocean sector background (median and uncertainty) also shown as in Fig. S2.

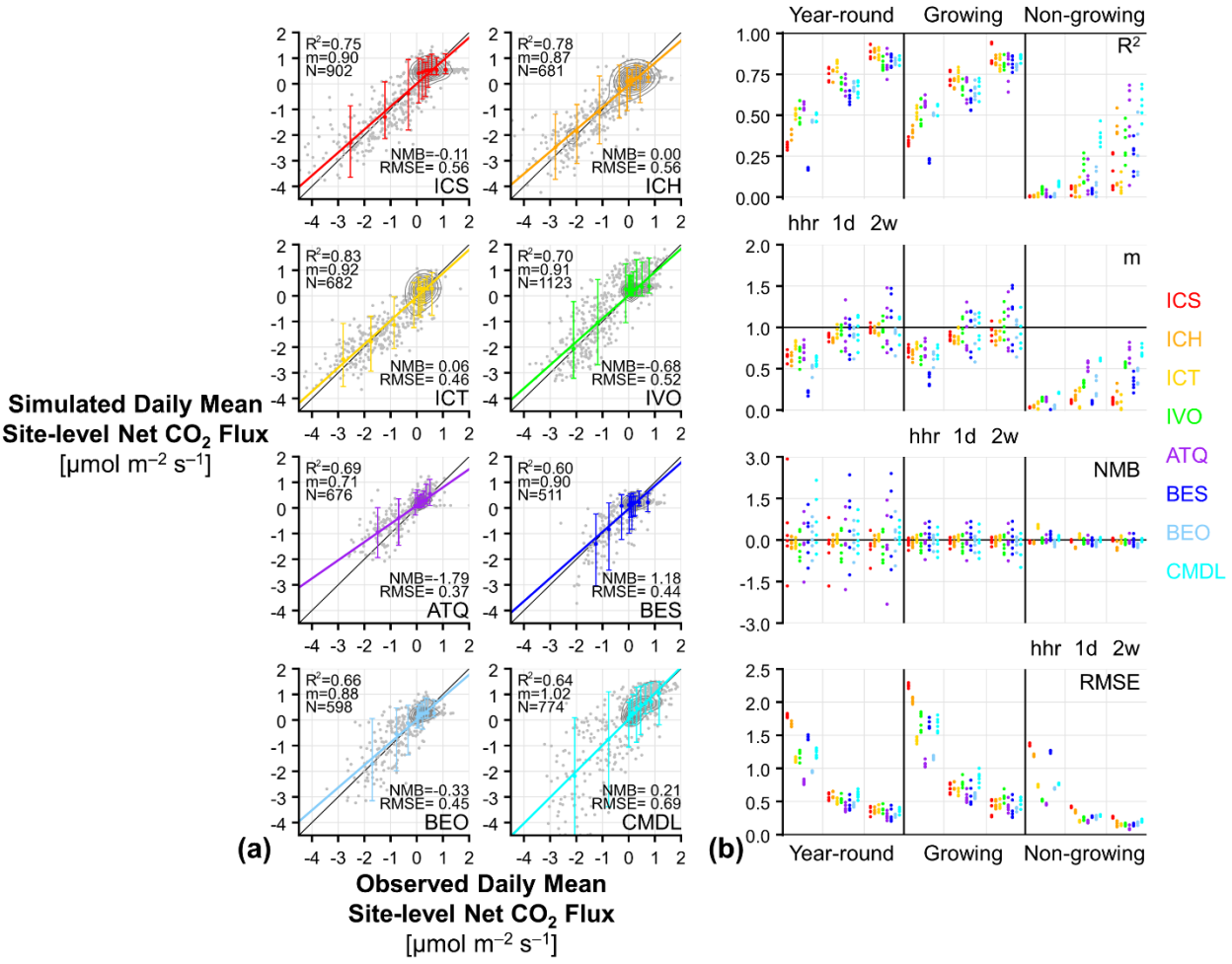

Figure S4. (a) Comparison of observed and simulated TPVRM daily mean site-level net CO_2 flux (gray dots) for 2013-2017 at eddy flux measurement sites used to determine TVPRM parameters, where TVPRM is driven by ERA5 meteorology and the CSIF SIF product. In each comparison, contours contain 10% of all points, and vertical bars indicate 95% distribution and colored dots indicate median of simulated values within each 10% bin of observations. Statistics shown for each comparison include coefficient of determination of all points (R^2), slope (m) determined by ordinary least squares using median of each 10% bin of observations, number of points (N), normalized mean bias (NMB) of all points, and root-mean-square error (RMSE) of all points. 1:1 line shown in dark gray. **(b)** Comparison statistics as in **(a)** for various TVPRM environmental drivers (six combinations of NARR and ERA5 meteorology with GOME-2, GOSIF, and CSIF SIF) over various averaging lengths (half-hour (hhr), one day (1d), two weeks (2w)) for various timeframes (year-round, growing season, non-growing season). Optimal value for each statistic shown as horizontal black line.

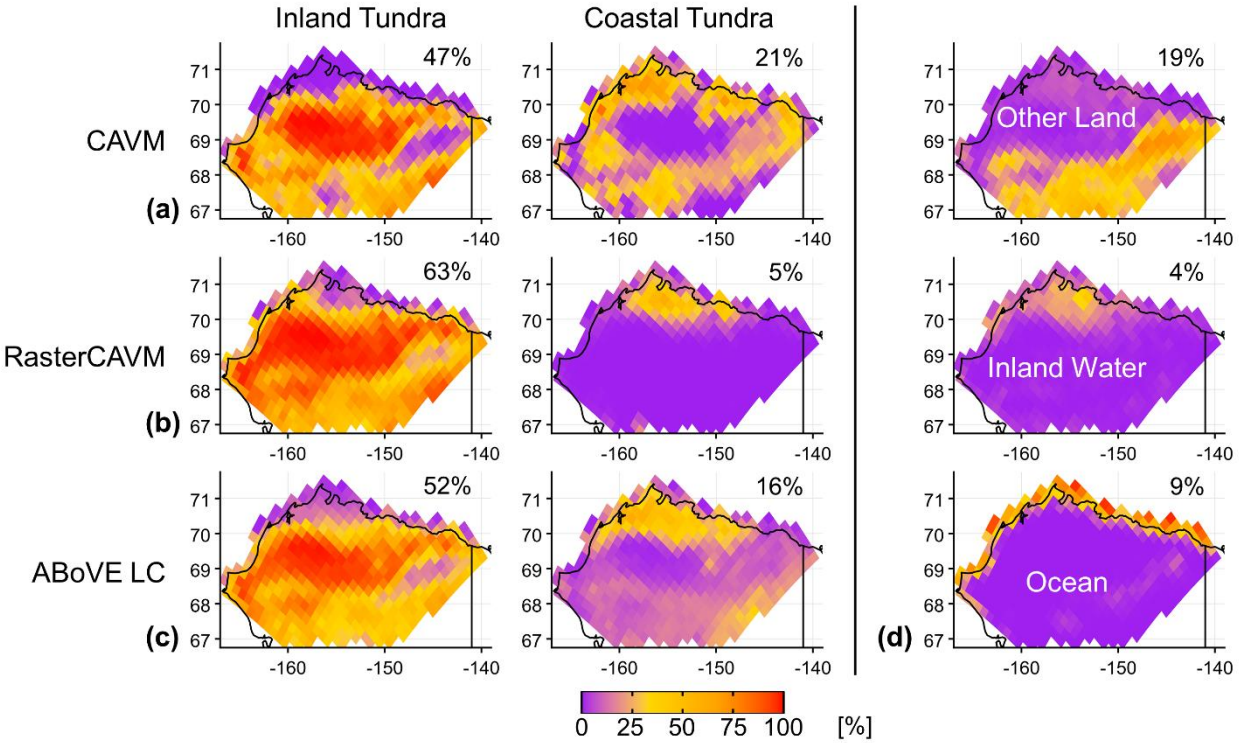

Figure S5. Spatial distribution of **(a)**–**(c)** inland and coastal tundra classification for (a) CAVM, (b) RasterCAVM, and (c) ABoVE LC vegetation maps and (d) other land, inland water, and ocean classifications for ABoVE LC vegetation map. Percentage of Alaska North Slope domain represented by each classification in upper right.

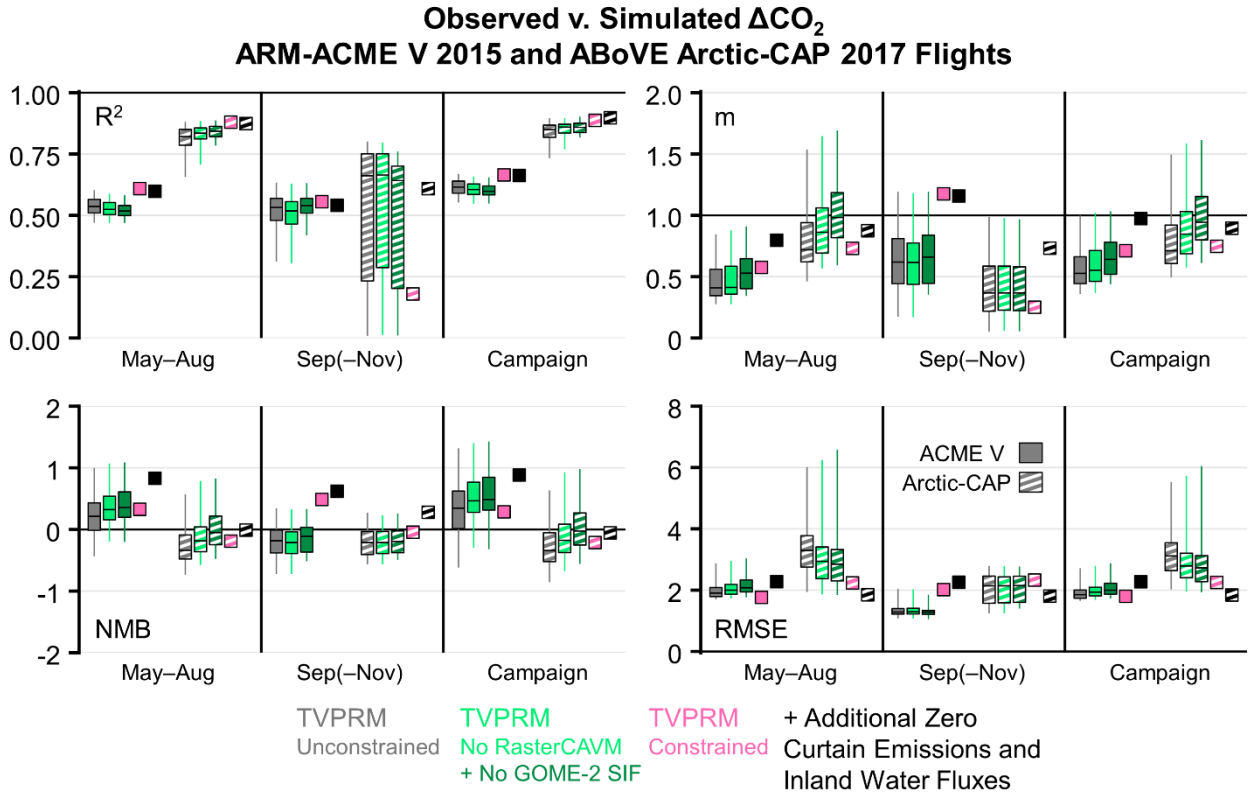

Figure S6. Statistics for comparison of observed and simulated ΔCO_2 during the ARM-ACME V and (solid fill) ABoVE Arctic-CAP (striped fill) aircraft campaign for various segments of the TVPRM ensemble (see legend) for various timeframes (growing season (May–Aug), early cold season (Sep(–Nov, ABoVE Arctic-CAP only)), entire campaign). Each comparison includes the coefficient of determination of all points (R^2), slope (m) determined by ordinary least squares using median of each 10% bin of observations, normalized mean bias (NMB) of all points, and root-mean-square error (RMSE) of all points. Optimal value for each statistic shown as horizontal black line.

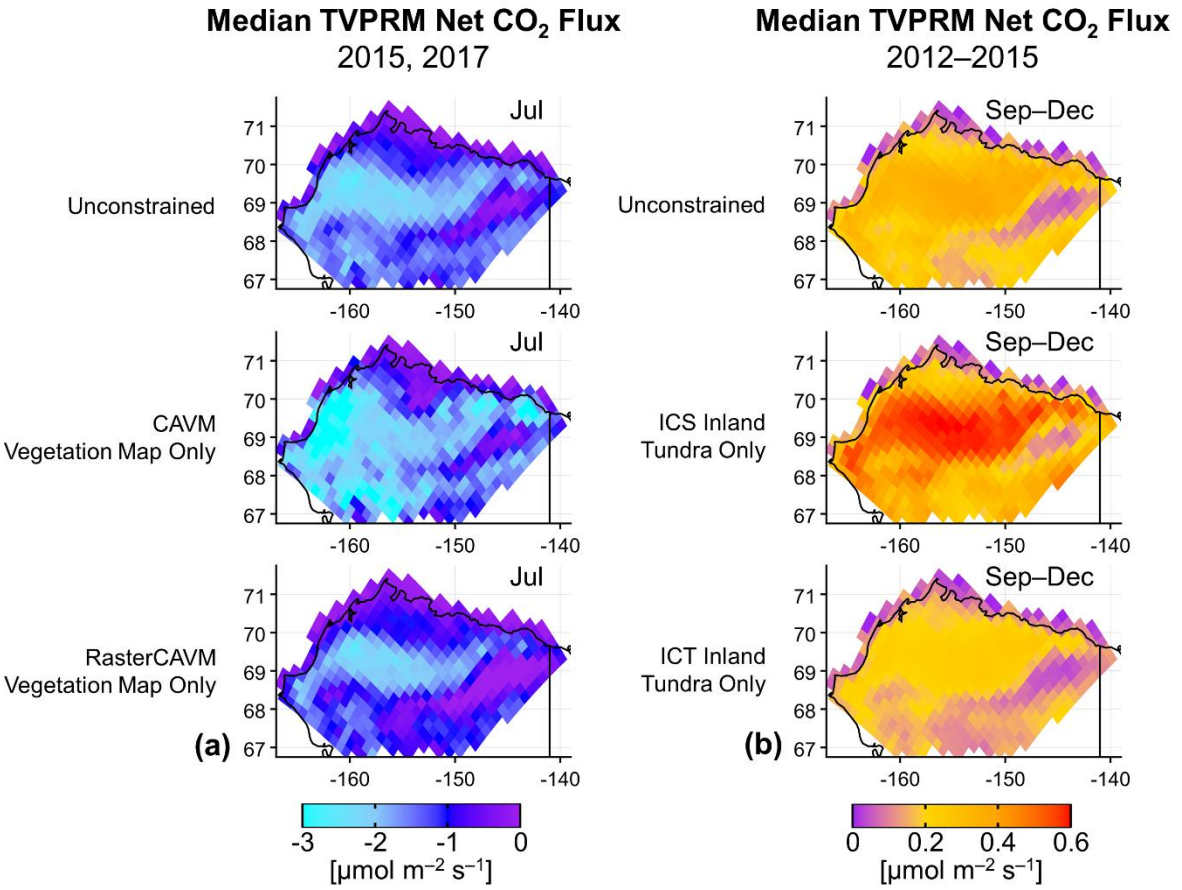

Figure S7. (a) Spatial distribution of mean July TVPRM net CO_2 flux for 2015 and 2017. Median value is shown for multiple TPVRM members using all vegetation maps (top), only CAVM vegetation map (middle), and only RasterCAVM vegetation map (bottom). Colors are saturated at –3 µmol m^{-2} s^{-1}. (b) Spatial distribution of mean Sep–Dec TVPRM net CO_2 flux for 2012–2015. Median value is shown for multiple TVPRM members using all inland site parameterizations (top), only ICS inland site parameterization (middle), and only ICT inland site parameterization (bottom). Colors are saturated at 0.6 µmol m^{-2} s^{-1}.

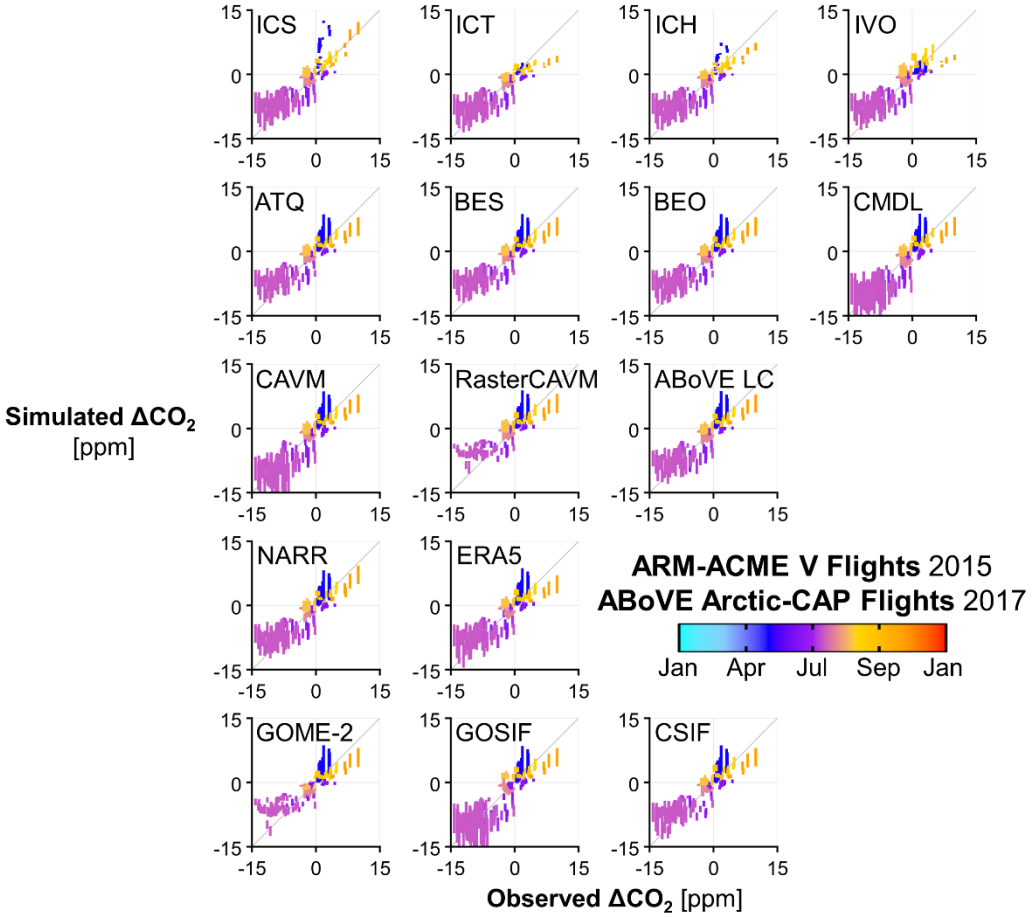

Figure S8. Comparison of vertically binned median observed and TVPRM simulated ΔCO_2 during the ARM-ACME V and ABoVE Arctic-CAP flight campaigns over the Alaska North Slope isolated for each model parameterization or driver. All points colored by day of year. Vertical boxes represent 50% of ΔCO_2 values from remaining TVPRM members from all binned points. 1:1 line shown in dark gray.

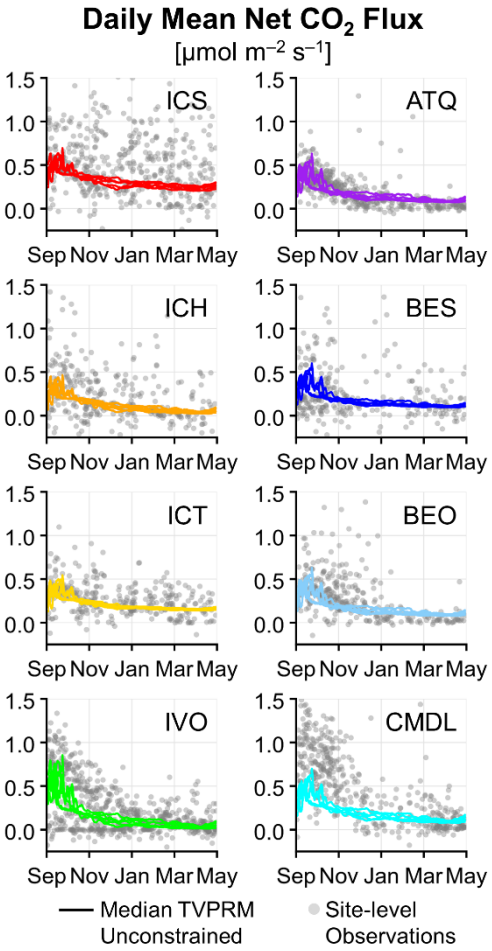

Figure S9. Observed daily mean site-level (grey points) and simulated daily mean Alaska North Slope (colored lines) net CO_2 flux at eight eddy flux sites for cold seasons (Sep–Apr) of 2012–2017. Simulated net CO_2 flux is for the median of all unconstrained TVPRM ensemble members using the observation-derived parameterizations from that eddy flux site.

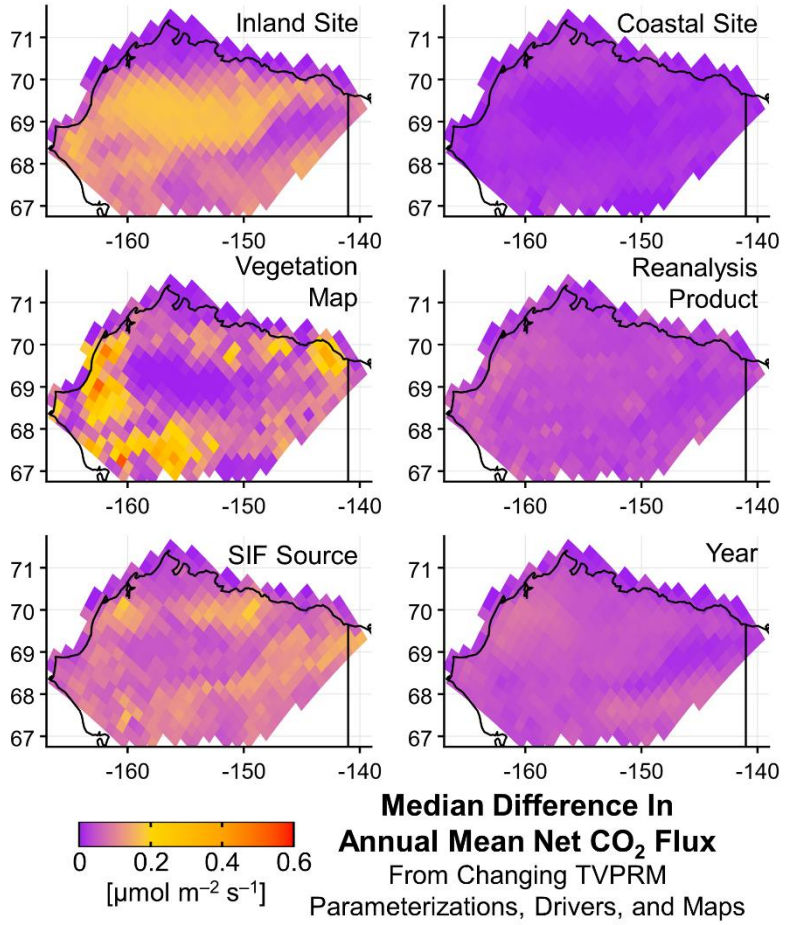

Figure S10. Spatial distribution of median difference in annual mean net CO_2 flux change driven by changing unconstrained TVPRM ensemble site-level parameterizations, environmental drivers, and vegetation distributions for 2012–2017 on the Alaska North Slope. Colors are saturated at 0.6 µmol m^{-2} s^{-1}.

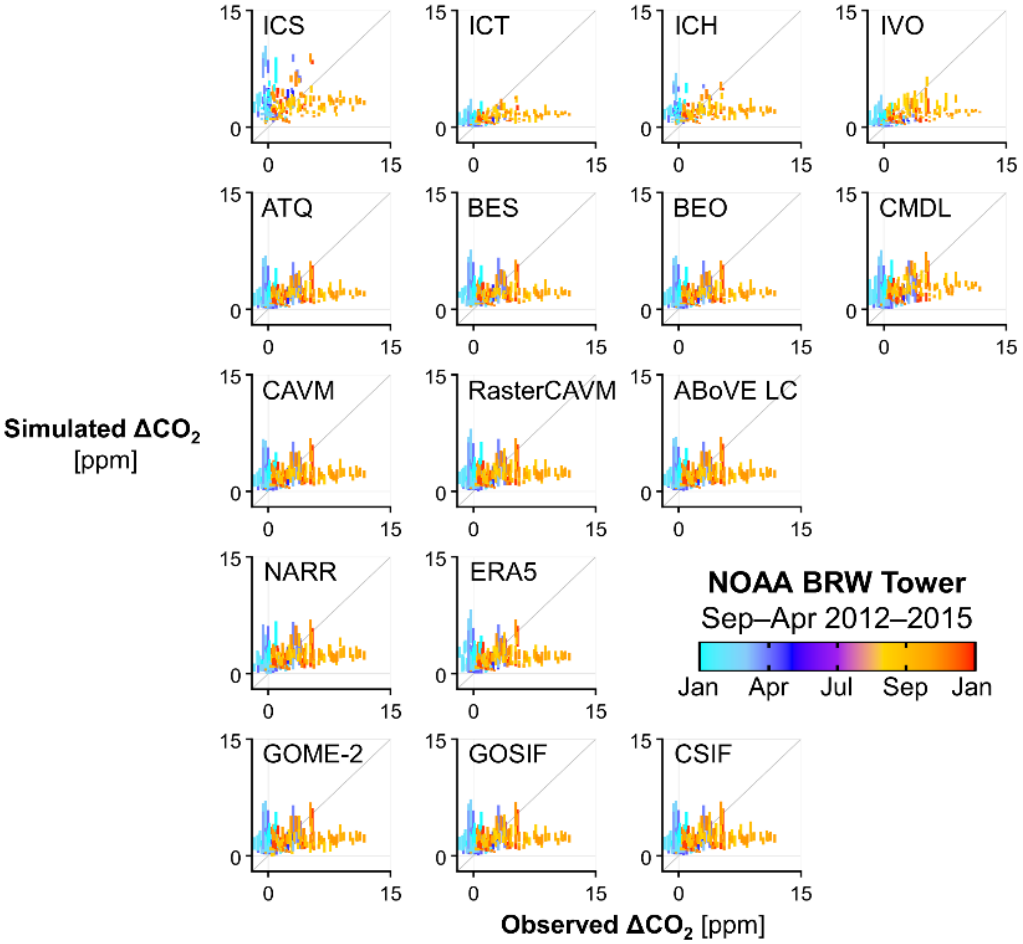

Figure S11. Comparison of hourly cold season (Sep–Apr) observed and TVPRM simulated ΔCO_2 at the NOAA BRW tower isolated for each model parameterization or driver. All points colored by day of year. Vertical boxes represent 50% of ΔCO_2 values from remaining TVPRM members. 1:1 line shown in dark gray.

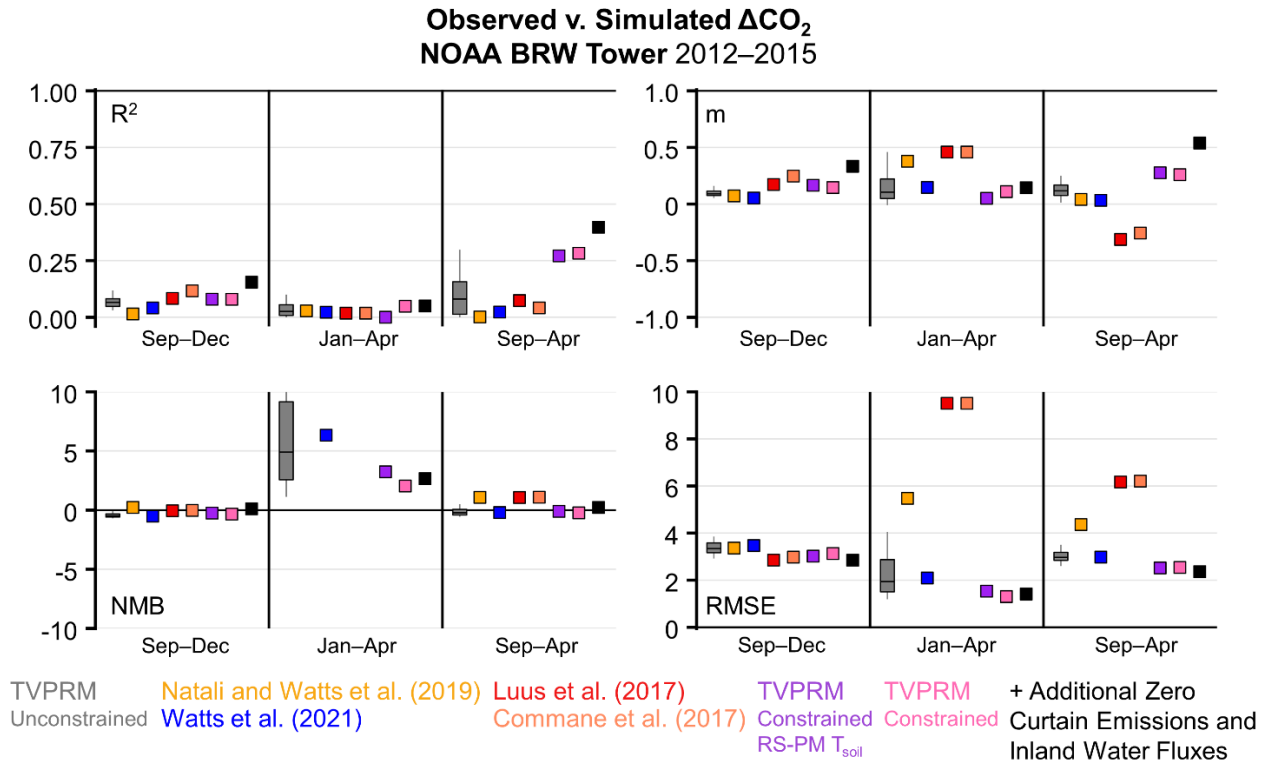

Figure S12. Statistics for comparison of observed and simulated ΔCO_2 at the NOAA BRW tower for various CO_2 flux models (see legend) for various timeframes (early cold season (Sep–Dec), late cold season (Jan–Apr), entire cold season (Sep–Apr)). Each comparison includes the coefficient of determination of all points (R^2), slope (m) determined by ordinary least squares using median of each 10% bin of observations, normalized mean bias (NMB) of all points, and root-mean-square error (RMSE) of all points. Optimal value for each statistic shown as horizontal black line.

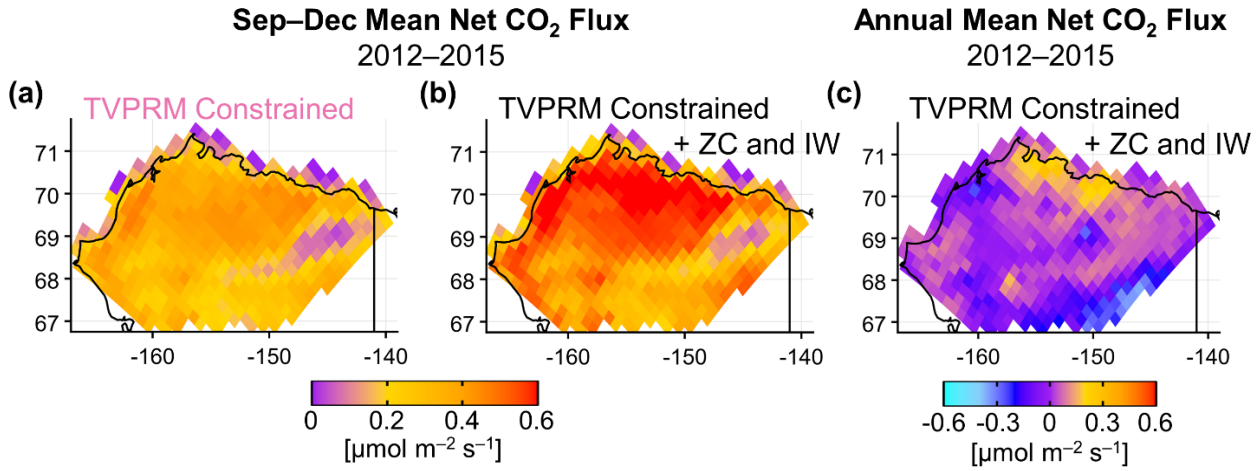

Figure S13. (a)–(b) Spatial distribution of early cold season (Sep–Dec) mean TVPRM net CO_2 flux for 2012–2015 for constrained TVPRM member + additional zero-curtain emissions (ZC) and inland water fluxes (IW). Colors are saturated at 0.6 μmol m^{-2} s^{-1}. (c) Spatial distribution of annual mean constrained TVPRM member + ZC and IW net CO_2 flux for 2012–2015. Colors are saturated at +/–0.6 μmol m^{-2} s^{-1}.

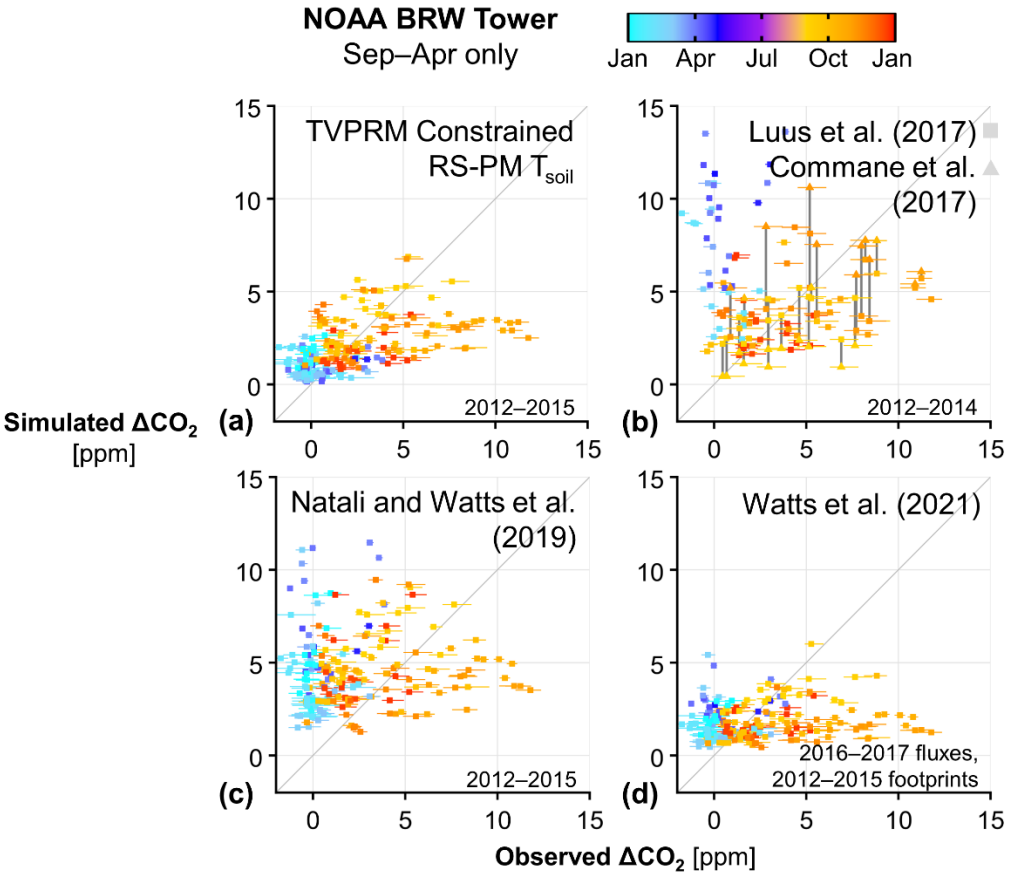

Figure S14. Comparison of hourly cold season (Sep–Apr) observed and simulated ΔCO_2 at the NOAA BRW tower using various CO_2 flux models and timeframes. All points colored by day of year. Horizontal segments indicate range of uncertainty in the BRW tower ocean sector background calculation. For (b), vertical gray bars connect corresponding points in the net CO_2 flux model values from Luus et al. (2017) and Commane et al. (2017). 1:1 line shown in dark gray.

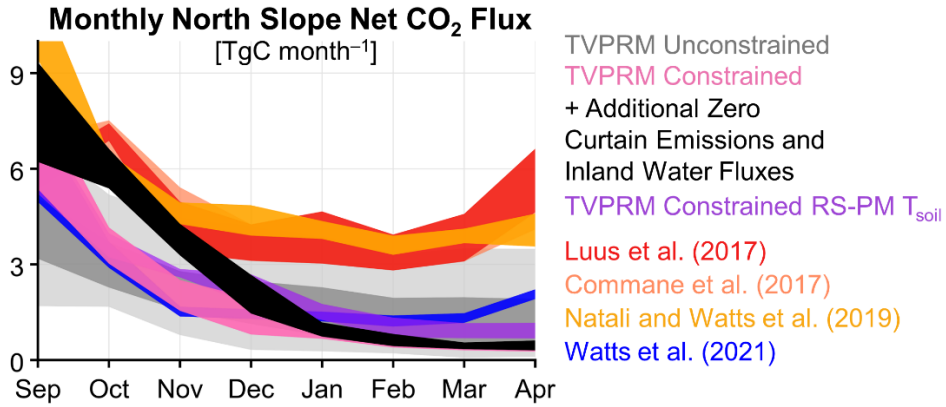

Figure S15. Monthly cold season total Alaska North Slope CO_2 fluxes for various CO_2 flux models shown in Figs. 4 and S14. The net CO_2 fluxes from the TVPRM ensemble and members and from Natali and Watts et al. (2019) show values for 2012–2017, from Luus et al. (2017) and Commane et al. (2017) show 2012–2014, and from Watts et al. (2021) show Sep 2016–Apr 2017. Ribbons represent range of all years, where applicable, except for unconstrained TVPRM ensemble, where dark gray ribbon represents 50% and light gray ribbon represents 95% of CO_2 flux values from all members for 2012–2017. Area of North Slope domain used to calculate regional totals is 3.537×10^5 km^2.

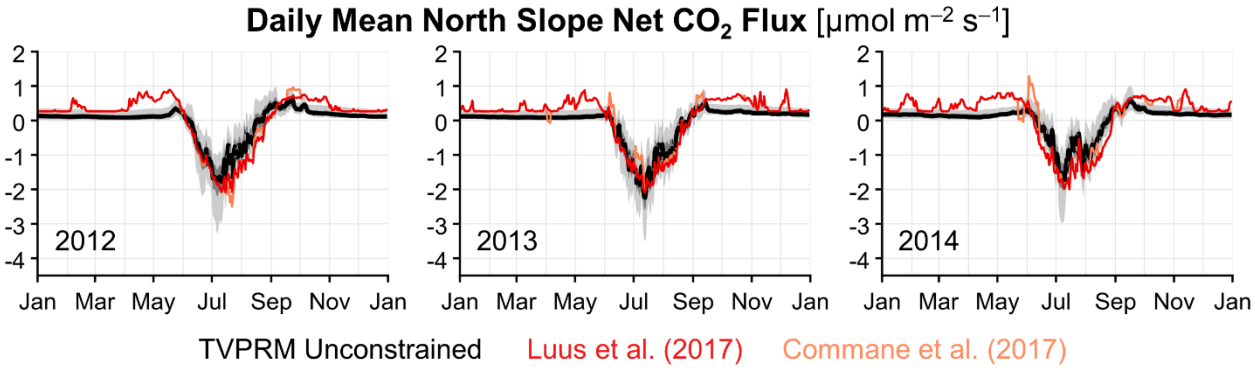

Figure S16. Timeseries of simulated daily mean Alaska North Slope net CO_2 flux for 2012–2014. Black line indicates median, dark gray ribbon represents 50%, and light gray ribbon represents 95% of daily mean net CO_2 flux values from all members of unconstrained TVPRM ensemble. Light red and dark red lines indicate daily mean net CO_2 flux values from Luus et al. (2017) and Commane et al. (2017), respectively.

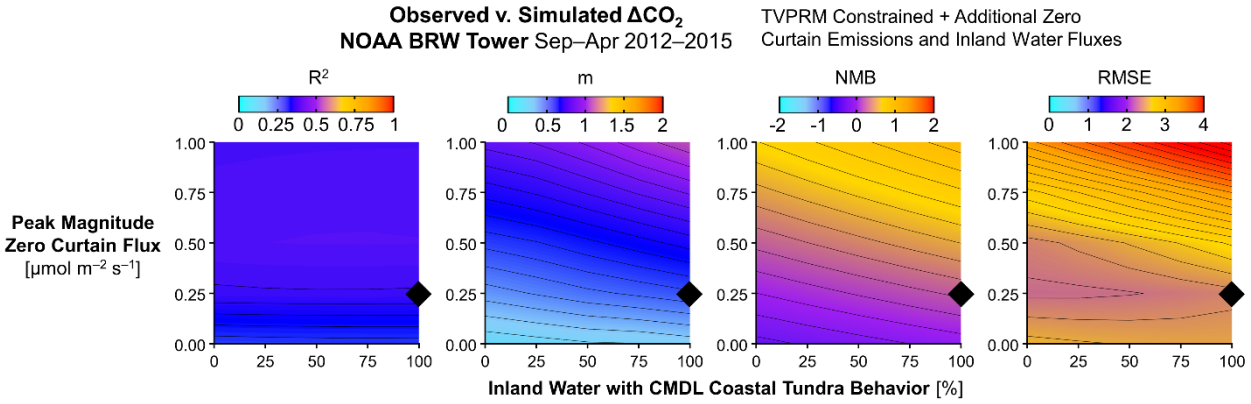

Figure S17. Statistics for comparison of observed and simulated ΔCO_2 at the NOAA BRW tower for the cold season (Sep–Apr) as calculated in Fig. S12. Simulated ΔCO_2 is determined using the constrained TVPRM member with varying amounts of inland water (IW) area represented as CMDL coastal tundra site parameterization (horizontal axis) and additional peak zero curtain (ZC) flux (vertical axis). Black diamonds indicate best performing combination and choice for ZC+IW formulation. Colors are saturated at shown colorbar endpoints.

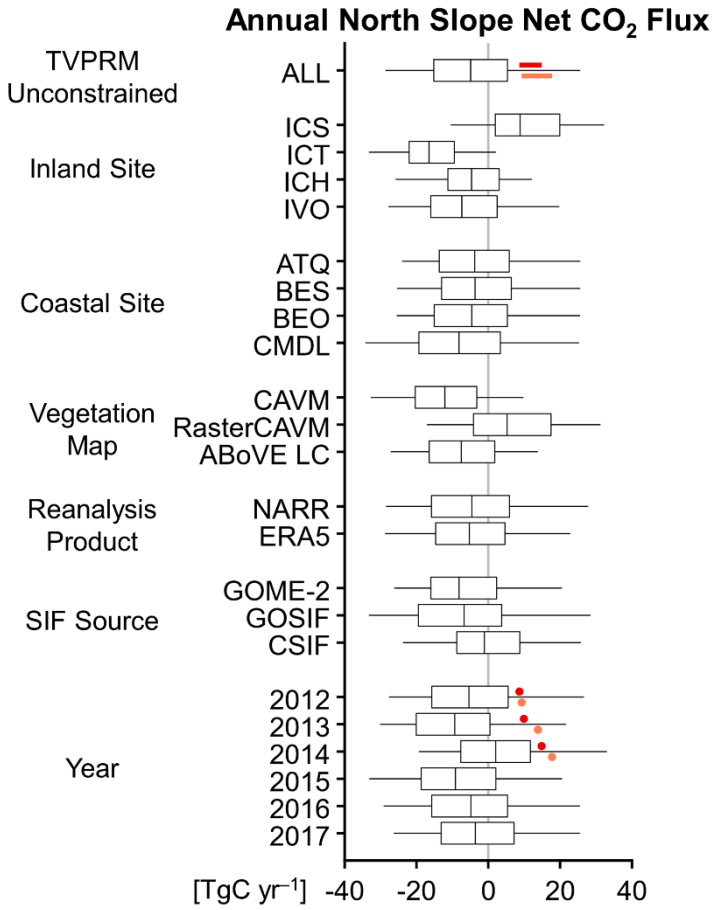

Figure S18. Range of annual North Slope net CO_2 flux from the TVPRM ensemble determined by various ecological parameterizations, environmental drivers, and vegetation distributions for 2012–2017 (black) and from the net CO_2 flux models by Luus et al. (2017) (dark red) and Commane et al. (2017) (light red) for 2012–2014. For each site parameterization or driver, boxes represent 50% and whiskers represent 95% of the net CO_2 flux from all TVPRM members included in that category. Area of North Slope domain used to calculate regional totals is 3.537×10^5 km^2.

Table S1. Annual and seasonal CO2 emission totals from anthropogenic and biomass burning sources and area burned in the Alaska North Slope and all of Alaska for 2012–2017. Annual anthropogenic emissions are from EDGAR, the Emissions Database for Global Atmospheric Research v7.0 (https://edgar.jrc.ec.europa.eu/dataset_ghg70). Monthly biomass burning emissions are from GFED, Global Fire Emissions Database v4 (https://globalfiredata.org/pages/data/#emissions). Area burned data is from the Alaska Interagency Coordination Center via UAF SNAP tool (https://snap.uaf.edu/tools/daily-fire-tally).

Dataset	Domain	2012	2013	2014	2015	2016	2017	Jun-Sep 2015	May-Nov 2017
Anthropogenic CO_2 Emissions [TgC]	North Slope	0.73	0.74	0.78	0.82	0.77	0.79		
	Alaska	7.7	7.7	7.8	8.2	8.3	8.4		
Biomass Burning CO_2 Emissions [TgC]	North Slope	0.23	0.12	0.00	0.12	0.34	0.07	0.12	0.07
	Alaska	0.97	6.7	1.7	28	1.9	7.6	28	7.6
Area Burned [million acres]	Alaska		1.3		5.1	0.50	0.65	5.1	0.65

Table S2. Alaska North Slope eddy covariance flux sites measuring net CO_2 flux for 2013-2017 used in this study. See Figs. 1c and S1 for map of site locations. ATQ, BES, BEO, CMDL, and IVO are further described by Zona et al. (2016) and Arndt et al. (2020). ICS, ICT, and ICH are further described by Euskirchen et al. (2012) and Euskirchen et al. (2017).

Site ID	Name	Ecosystem / TVPRM Group	Vegetation	Data Coverage (month/year)
ATQ	Atqasuk	Wet polygonised tundra / coastal	Water sedge, dwarf shrub	09/2013–11/2013, 02/2014–10/2014, 02/2015–01/2016, 07/2016, 09/2016–04/2017, 06/2017–07/2017, 09/2017–12/2017
BES	Barrow Biocomplexity Experiment, South	Wetland tundra / coastal	Sedge, moss	07/2013–11/2014, 02/2015–10/2015, 07/2016–01/2017, 05/2017–07/2017
BEO	Barrow Environmental Observatory	Wet polygonised tundra / coastal	Graminoid grass, sedge	09/2013–01/2015, 06/2015–02/2016, 04/2016–07/2016, 07/2017–12/2017
CMDL	Barrow Climate Monitoring and Diagnostics Laboratory	Moist tundra / coastal	Graminoid grass, lichen	10/2013–10/2014, 02/2015–05/2015, 07/2015–09/2017, 11/2017–12/2017
IVO	Ivotuk	Tussock tundra / inland	Tussock-forming sedge, moss	06/2013–11/2014, 02/2015–12/2017
ICS	Imnavait Creek Wet Sedge	Wet sedge tundra / inland	Water sedge, swarf deciduous shrub, moss	01/2013–12/2017
ICH	Imnavait Creek Heath Tundra	Dry heath tundra / inland	Dwarf evergreen shrub, deciduous shrub, lichen	01/2013–12/2016, 03/2017–12/2017
ICT	Imnavait Creek Tussock Tundra	Moist acidic tussock tundra / inland	Tussock-forming sedge, deciduous dwarf shrub, evergreen dwarf shrub	01/2013–12/2014, 04/2015–12/2017

Table S3. Previously developed CO_2 flux models used in this study.

Model ID	Model Resolution / Years	Model Details
Luus et al. (2017)	1/4° × 1/6° spatial, 3 hourly temporal / 2012–2014	Similar to TPVRM, using monthly SIF values and alternative eddy flux sites and methods to calculate variable parameters. Accounts for both boreal and tundra ecosystems.
Commane et al. (2017)	0.5° spatial, 3 hourly temporal / 2012–2014	Luus et al. (2017) optimized based on observations from the Carbon in Arctic Reservoirs Vulnerability Experiment (CARVE) flight campaign. Reverts to Luus et al. (2017) for time periods without flights.
Natali and Watts et al. (2019)	25 km spatial, monthly temporal / 2012–2015	Synthesis of pan-Arctic winter in situ CO_2 flux observations and environmental drivers using boosted regression tree machine learning.
Watts et al. (2021)	300 m spatial, monthly temporal / 2016–2017	Integration of Alaskan and northwest Canadian belowground CO_2 flux observations and satellite data using random forest machine learning.

Table S4. Reanalysis meteorology products for 2012-2017 used by TVPRM in this study.

Met ID	Product Name	Product Resolution	Product Variable used in TVPRM		
			T_a	T_s	PAR
NARR	NOAA North American Regional Reanalysis Mesinger et al. (2006)	~30 km spatial, 3 hourly temporal	air.2m	tsoil (10 cm)	dswrf
ERA5	ECMWF Reanalysis, fifth generation Hersbach et al. (2020)	~31 km spatial, hourly temporal	t2m	stl2 (7–28 cm)	ssrd

Table S5. SIF products for 2012-2017 used by TVPRM in this study.

SIF ID	Product Name	Product Resolution	Product Details
GOME-2	Interpolated GOME-2 SIF (created for this study) [GOME-2: Global Ozone Monitoring Experiment-2]	0.01° latitudinal, daily temporal	Discrete GOME-2 SIF v27 retrievals (Joiner et al., 2016), normalized by solar zenith angle, averaged by center point into overlapping 0.5° latitudinal bins across the North Slope domain. Temporal interpolation within each bin and latitudinal interpolation across bins applied using loess fit smoothing.
GOSIF	Global 'OCO-2' SIF (Li and Xiao, 2019) [OCO-2: Orbiting Carbon Observatory-2]	0.05° spatial, 8 day temporal	Aggregated OCO-2 soundings combined with MODIS enhanced vegetation index and MERRA-2 PAR, vapor pressure deficit, and air temperature to create a higher resolution gridded SIF product using multivariate linear regression.
CSIF	Contiguous SIF (Zhang et al., 2018)	0.05° spatial, 4 day temporal	Aggregated OCO-2 soundings combined with MODIS surface reflectance to create a higher resolution gridded SIF product using a neural network.

Table S6. Vegetation maps used by TVPRM in this study.

Map ID	Map Name	Map Resolution / Year	Map Classification Details
CAVM	Circumpolar Arctic Vegetation Map (Walker et al., 2005)	14 km polygons, 8 km linear features / satellite data from 1993 and 1995, developed in 2003	15 classification units based on plant growth forms, roughly separated by summer temperature and soil moisture. Polygon classification from combination of satellite, vegetation, temperature, topographic, and geologic data.
RasterCAVM	Raster version of CAVM (Raynolds et al., 2019)	1 km spatial / satellite data as in CAVM, additional data from 2000–2009	Classification as in CAVM, redistributed at higher resolution based on unsupervised classification using satellite and elevation data.
ABoVE LC	Landsat-derived Annual Dominant Land Cover across ABoVE Core Domain (Wang et al., 2020)	30 m spatial / 2014 [ABoVE: Arctic-Boreal Vulnerability Experiment]	15 classification units based on semi-supervised classification using satellite, climate, and topographic data

Table S7. Alaska North Slope growing season (May–Aug) net CO_2 flux by component for the TVPRM Constrained + ZC and IW scenario for 2012–2017.

Flux Component	2012	2013	2014	2015	2016	2017
R_{soil} [TgC]	18	16	17	18	18	17
R_{plant} [TgC]	33	30	28	33	33	30
GPP [TgC]	69	71	60	77	71	68
NEE [TgC]	-18	-25	-15	-25	-19	-21

Table S8. Alaska North Slope growing season (May-Aug) mean TVPRM drivers used in the TVPRM Constrained + ZC and IW scenario for 2012–2017, where the mean uses model gridboxes with a total ABoVE LC ocean and other land fraction of less than 0.5 (see Fig. S5).

Driver	2012	2013	2014	2015	2016	2017
NARR Ta [°C]	7.4	6.6	6.2	7.5	7.8	6.8
NARR T_{scale} [0-1]	0.67	0.61	0.58	0.65	0.65	0.58
NARR Ts [°C]	2.6	0.68	1.3	2.4	2.7	1.5
NARR PAR [µmol photon m^{-2} s^{-1}]	484	478	466	495	497	507
CSIF SIF product [mW m^{-2} nm^{-1} sr^{-1}]	0.17	0.18	0.16	0.19	0.18	0.18

Table S9. Alaska North Slope growing season (May-Aug) mean additional select NARR Variables for 2012–2017, where the mean uses model gridboxes with a total ABoVE LC ocean and other land fraction of less than 0.5 (see Fig. S5).

Variable	2012	2013	2014	2015	2016	2017
NARR 3hr accumulated precipitation [kg m^{-2}]	0.19	0.21	0.20	0.15	0.16	0.16
NARR soil moisture content [kg m^{-2}]	688	745	755	747	733	734
NARR snow depth [m]	0.046	0.076	0.032	0.030	0.026	0.040
NARR snow cover fraction [0-1]	0.15	0.20	0.16	0.12	0.11	0.17
NARR snow depth [m] during proceeding Sep-Apr	0.42	0.35	0.36	0.38	0.35	0.38
NARR snow cover fraction [0-1] during proceeding Sep-Apr	0.81	0.78	0.79	0.83	0.87	0.78

References

Arndt, K. A., Lipson, D. A., Hashemi, J., Oechel, W. C., and Zona, D.: Snow melt stimulates ecosystem respiration in Arctic ecosystems, Global Change Biol., 26, 5042–5051, https://doi.org/10.1111/gcb.15193, 2020.

Commane, R., Lindaas, J., Benmergui, J., Luus, K. A., Chang, R. Y.-W., Daube, B. C., Euskirchen, E. S., Henderson, J. M., Karion, A., Miller, J. B., Miller, S. M., Parazoo, N. C., Randerson, J. T., Sweeney, C., Tans, P., Thoning, K., Veraverbeke, S., Miller, C. E., and Wofsy, S. C.: Carbon dioxide sources from Alaska driven by increasing early winter respiration from Arctic tundra, PNAS, 114, 5361–5366, https://doi.org/10.1073/pnas.1618567114, 2017.

Euskirchen, E. S., Bret-Harte, M. S., Scott, G. J., Edgar, C., and Shaver, G. R.: Seasonal patterns of carbon dioxide and water fluxes in three representative tundra ecosystems in northern Alaska, Ecosphere, 3, art4, https://doi.org/10.1890/ES11-00202.1, 2012.

Euskirchen, E. S., Bret-Harte, M. S., Shaver, G. R., Edgar, C. W., and Romanovsky, V. E.: Long-Term Release of Carbon Dioxide from Arctic Tundra Ecosystems in Alaska, Ecosystems, 20, 960–974, https://doi.org/10.1007/s10021-016-0085-9, 2017.

Hersbach, H., Bell, B., Berrisford, P., Hirahara, S., Horányi, A., Muñoz-Sabater, J., Nicolas, J., Peubey, C., Radu, R., Schepers, D., Simmons, A., Soci, C., Abdalla, S., Abellan, X., Balsamo, G., Bechtold, P., Biavati, G., Bidlot, J., Bonavita, M., Chiara, G. D., Dahlgren, P., Dee, D., Diamantakis, M., Dragani, R., Flemming, J., Forbes, R., Fuentes, M., Geer, A., Haimberger, L., Healy, S., Hogan, R. J., Hólm, E., Janisková, M., Keeley, S., Laloyaux, P., Lopez, P., Lupu, C., Radnoti, G., Rosnay, P. de, Rozum, I., Vamborg, F., Villaume, S., and Thépaut, J.-N.: The ERA5 global reanalysis, Q. J. Roy. Meteorol. Soc., 146, 1999–2049, https://doi.org/10.1002/qj.3803, 2020.

Joiner, J., Yoshida, Y., Guanter, L., and Middleton, E. M.: New methods for the retrieval of chlorophyll red fluorescence from hyperspectral satellite instruments: simulations and application to GOME-2 and SCIAMACHY, Atmos. Meas. Tech., 9, 3939–3967, https://doi.org/10.5194/amt-9-3939-2016, 2016.

Li, X. and Xiao, J.: A Global, 0.05-Degree Product of Solar-Induced Chlorophyll Fluorescence Derived from OCO-2, MODIS, and Reanalysis Data, Remote Sens., 11, 517, https://doi.org/10.3390/rs11050517, 2019.

Luus, K. A., Commane, R., Parazoo, N. C., Benmergui, J., Euskirchen, E. S., Frankenberg, C., Joiner, J., Lindaas, J., Miller, C. E., Oechel, W. C., Zona, D., Wofsy, S., and Lin, J. C.: Tundra photosynthesis captured by satellite-observed solar-induced chlorophyll fluorescence, Geophys. Res. Lett., 44, 2016GL070842, https://doi.org/10.1002/2016GL070842, 2017.

Mesinger, F., DiMego, G., Kalnay, E., Mitchell, K., Shafran, P. C., Ebisuzaki, W., Jović, D., Woollen, J., Rogers, E., Berbery, E. H., Ek, M. B., Fan, Y., Grumbine, R., Higgins, W., Li, H., Lin, Y., Manikin, G., Parrish, D., and Shi, W.: North American Regional Reanalysis, B. Am. Meteorol. Soc., 87, 343–360, https://doi.org/10.1175/BAMS-87-3-343, 2006.

Natali, S. M., Watts, J. D., Rogers, B. M., Potter, S., Ludwig, S. M., Selbmann, A.-K., Sullivan, P. F., Abbott, B. W., Arndt, K. A., Birch, L., Björkman, M. P., Bloom, A. A., Celis, G., Christensen, T. R., Christiansen, C. T., Commane, R., Cooper, E. J., Crill, P., Czimczik, C., Davydov, S., Du, J., Egan, J. E., Elberling, B., Euskirchen, E. S., Friborg, T., Genet, H., Göckede, M., Goodrich, J. P., Grogan, P., Helbig, M., Jafarov, E. E., Jastrow, J. D., Kalhori, A. A. M., Kim, Y., Kimball, J. S., Kutzbach, L., Lara, M. J., Larsen, K. S., Lee, B.-Y., Liu, Z., Loranty, M. M., Lund, M., Lupascu, M., Madani, N., Malhotra, A., Matamala, R., McFarland, J., McGuire, A. D., Michelsen, A., Minions, C., Oechel, W. C., Olefeldt, D., Parmentier, F.-J. W., Pirk, N., Poulter, B., Quinton, W., Rezanezhad, F., Risk, D., Sachs, T., Schaefer, K., Schmidt, N. M., Schuur, E. A. G., Semenchuk, P. R., Shaver, G., Sonnentag, O., Starr, G., Treat, C. C., Waldrop, M. P., Wang, Y., Welker, J., Wille, C., Xu, X., Zhang, Z., Zhuang, Q., and Zona, D.: Large loss of CO 2 in winter observed across the northern permafrost region, Nat. Clim. Change, 9, 852–857, https://doi.org/10.1038/s41558-019-0592-8, 2019.

Raynolds, M. K., Walker, D. A., Balser, A., Bay, C., Campbell, M., Cherosov, M. M., Daniëls, F. J. A., Eidesen, P. B., Ermokhina, K. A., Frost, G. V., Jedrzejek, B., Jorgenson, M. T., Kennedy, B. E., Kholod, S. S., Lavrinenko, I. A., Lavrinenko, O. V., Magnússon, B., Matveyeva, N. V., Metúsalemsson, S., Nilsen, L., Olthof, I., Pospelov, I. N., Pospelova, E. B., Pouliot, D., Razzhivin, V., Schaepman-Strub, G., Šibík, J., Telyatnikov, M. Yu., and Troeva, E.: A raster version of the Circumpolar Arctic Vegetation Map (CAVM), Remote Sens. Environ., 232, 111297, https://doi.org/10.1016/j.rse.2019.111297, 2019.

Walker, D. A., Raynolds, M. K., Daniëls, F. J. A., Einarsson, E., Elvebakk, A., Gould, W. A., Katenin, A. E., Kholod, S. S., Markon, C. J., Melnikov, E. S., Moskalenko, N. G., Talbot, S. S., Yurtsev, B. A. (†), and Team, T. other members of the C.: The Circumpolar Arctic vegetation map, J. Veg. Sci., 16, 267–282, https://doi.org/10.1111/j.1654-1103.2005.tb02365.x, 2005.

Wang, J. A., Sulla-Menashe, D., Woodcock, C. E., Sonnentag, O., Keeling, R. F., and Friedl, M. A.: Extensive land cover change across Arctic–Boreal Northwestern North America from disturbance and climate forcing, Global Change Biol., 26, 807–822, https://doi.org/10.1111/gcb.14804, 2020.

Watts, J. D., Natali, S. M., Minions, C., Risk, D., Arndt, K., Zona, D., Euskirchen, E. S., Rocha, A. V., Sonnentag, O., Helbig, M., Kalhori, A., Oechel, W., Ikawa, H., Ueyama, M., Suzuki, R., Kobayashi, H., Celis, G., Schuur, E. A. G., Humphreys, E., Kim, Y., Lee, B.-Y., Goetz, S., Madani, N., Schiferl, L. D., Commane, R., Kimball, J. S., Liu, Z., Torn, M. S., Potter, S., Wang, J. A., Jorgenson, M. T., Xiao, J., Li, X., and Edgar, C.: Soil respiration strongly offsets carbon uptake in Alaska and Northwest Canada, Environ. Res. Lett., 16, 084051, https://doi.org/10.1088/1748-9326/ac1222, 2021.

Yi, Y., Kimball, J. S., Chen, R. H., Moghaddam, M., Reichle, R. H., Mishra, U., Zona, D., and Oechel, W. C.: Characterizing permafrost active layer dynamics and sensitivity to landscape spatial heterogeneity in Alaska, Cryosphere, 12, 145–161, https://doi.org/10.5194/tc-12-145-2018, 2018.

Yi, Y., Kimball, J. S., Chen, R. H., Moghaddam, M., and Miller, C. E.: Sensitivity of active-layer freezing process to snow cover in Arctic Alaska, Cryosphere, 13, 197–218, https://doi.org/10.5194/tc-13-197-2019, 2019.

Zhang, Y., Joiner, J., Alemohammad, S. H., Zhou, S., and Gentine, P.: A global spatially contiguous solar-induced fluorescence (CSIF) dataset using neural networks, Biogeosciences, 15, 5779–5800, https://doi.org/10.5194/bg-15-5779-2018, 2018.

Zona, D., Gioli, B., Commane, R., Lindaas, J., Wofsy, S. C., Miller, C. E., Dinardo, S. J., Dengel, S., Sweeney, C., Karion, A., Chang, R. Y.-W., Henderson, J. M., Murphy, P. C., Goodrich, J. P., Moreaux, V., Liljedahl, A., Watts, J. D., Kimball, J. S., Lipson, D. A., and Oechel, W. C.: Cold season emissions dominate the Arctic tundra methane budget, PNAS, 113, 40–45, https://doi.org/10.1073/pnas.1516017113, 2016.